

## Air-sea gas transfer velocity for oxygen derived from float data

C. Kihm<sup>1</sup> and A. Körtzinger<sup>1</sup>

Received 28 December 2009; revised 13 July 2010; accepted 25 August 2010; published 2 December 2010.

[1] We estimated the air-sea gas transfer velocity for oxygen using 3 consecutive years (September 2003 to August 2006) of high-quality oxygen measurements from profiling floats in the central Labrador Sea. Mixed layer oxygen concentrations exhibit strong seasonality characterized by biologically and thermally driven evasion during spring/summer and invasion during fall/winter caused by cooling and ventilation of oxygen deficient subsurface waters. Mixed layer oxygen budgets entirely excluding the spring bloom period are employed to estimate the air-sea transfer velocity for oxygen. By using colocated wind speed data acquired by scatterometry from the QuikSCAT satellite, wind speed-dependent parameterizations for the air-sea gas transfer velocity  $k_{660}$  ( $\text{CO}_2$  at  $20^\circ\text{C}$  and salinity 35) are established and compared with prominent parameterizations from the literature. Quadratic, cubic, and quartic functions are fitted to the data for short-term and long-term wind speed averages separately. In both cases, the quadratic functions yield the poorest fit to the observations. Overall, the stronger curvature of the cubic functions provides the best fit, while the quartic function also fits the data less well. Our results generally confirm the stronger wind speed dependencies among the suite of published parameterizations. Also, the better fits found for cubic function point at the strong importance of very high wind speed for air-sea gas exchange of  $\text{O}_2$ .

**Citation:** Kihm, C., and A. Körtzinger (2010), Air-sea gas transfer velocity for oxygen derived from float data, *J. Geophys. Res.*, 115, C12003, doi:10.1029/2009JC006077.

### 1. Introduction

[2] For several decades, significant effort has gone into determining the relationship between the air-sea gas transfer velocity (also known as piston velocity) and wind speed. Using such a relationship in conjunction with the bulk equation for gas exchange, gas fluxes can be calculated from measured partial pressure differences, in our case of oxygen, and wind speed over the ocean. In this study we followed a mixed layer budget approach to determine the air-sea gas transfer velocity for oxygen in the convection region of the central Labrador Sea. Changes in the vertical mixed layer oxygen inventory between two consecutive oxygen profiles were interpreted to be generally dominated by air-sea exchange of oxygen. We entirely excluded the spring bloom period where this assumption is clearly violated due to high biological productivity and the concurrent production of oxygen. In the remaining data however, small-scale spatial variability is inevitably included in the analysis and creates considerable scatter in the obtained results.

### 2. Methods

#### 2.1. Oxygen Floats

[3] In this study we use dissolved oxygen concentrations measured by two profiling floats in the Labrador

Sea (Figure 1). Each float (APEX, Webb Research Inc., Falmouth, USA) was equipped with an oxygen optode sensor (Model 3830, Aanderaa Data Instruments, Bergen, Norway) as well as a SBE-41 CTD instrument (Sea-Bird Electronics Inc., Bellevue/WA, USA). During the floats ascent from its profiling depth (2000 dbar) to the surface, temperature, conductivity (salinity), pressure and oxygen are measured at 72 depth levels. At the surface the float transmits the collected data via the Argos satellite system and then dives to its drift (parking) depth of 800 dbar. This measurement cycle is repeated every 7 days. Float 4900607 was deployed on 7 September 2003 and float 4900611 on 15 September 2004. Following thorough quality control, 150 profiles from the two floats containing 61 to 72 vertical data points each were subjected to in the present analysis.

#### 2.2. Mixed Layer Depth

[4] Mixed layer depths (MLD) were estimated from vertical temperature, salinity and oxygen profiles measured by the two ARGO floats 4900607 and 4900611. The classical criteria of *Monterey and Levitus* [1997] for temperature ( $\Delta T = 0.5^\circ\text{C}$ ) as well as for density ( $\Delta \sigma = 0.125 \text{ kg m}^{-3}$ ) are not suitable in subpolar oceans. Employing these classical criteria caused significant overestimation of the mixed layer depth particularly during the winter period of deep convection when vertical gradients in  $T$  and  $\sigma$  nearly disappear. We therefore applied oxygen as a tracer for the estimation of the depth of the ventilated mixed layer as proposed by *Körtzinger et al.* [2008]. Where oxygen data were available, an oxygen difference criterion ( $\Delta \text{O}_2 = 5 \mu\text{mol L}^{-1}$ ) was applied to estimate mixed layer depth. Mixed layer depths  $>400 \text{ m}$

<sup>1</sup>Leibniz-Institut für Meereswissenschaften an der Universität Kiel, Kiel, Germany.

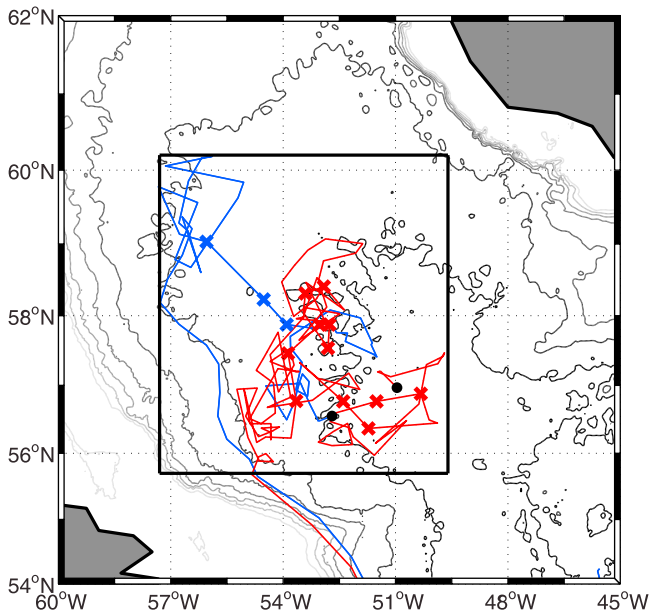


**Figure 1.** Trajectories of two APEX floats equipped with an Aanderaa oxygen optode (Model 3830, Aanderaa Data Instruments, Bergen, Norway) in the central Labrador Sea during the period September 2003–August 2006. The blue line shows the track of float 4900607 (14 September 2003 to 3 October 2004), and the red line shows the track of float 4900611 (13 October 2004 to 9 August 2006); the black dots denote the deployment positions. The drift depth of both floats was 800 dbar, and the profiling depth was 2000 dbar. This study only includes profiles taken within the rectangular box which marks the approximate location of the area of deep winter convection. The crosses indicate where mixed layer depths >600 m were found. The bathymetry contour interval is 500 dbar.

were additionally checked by visual inspection and ambiguous MLD values were replaced by the visually determined mixed layer depth of the oxygen profile. We also applied a modified classical criterion ( $\Delta\theta = 0.15^\circ\text{C}$  and  $\Delta\sigma_\theta = 0.03 \text{ kg m}^{-3}$ ) for comparison with the oxygen criterion. MLD estimates acquired this way agreed to within 12% ( $\text{MLD}_{\sigma_w}$ ) and 33% ( $\text{MLD}_\theta$ ) for  $\text{MLD} < 100 \text{ m}$  and 53% ( $\text{MLD}_{\sigma_w}$ ) and 46% ( $\text{MLD}_\theta$ ) for  $\text{MLD} > 100 \text{ m}$ , respectively. The deepest mixed layer depths observed by the profiling floats during the three winters (February–April) were 1350 m in 2003/2004, 710 m in 2004/2005, and 900 m in 2005/2006. Varying the applied oxygen criterion by  $\pm 1 \mu\text{mol L}^{-1}$  leads to a change of the determined mixed layer depth of  $\sim 15\%$  ( $\text{MLD} < 100 \text{ m}$ ) and  $\sim 9\%$  ( $\text{MLD} > 100 \text{ m}$ ). We therefore consider the MLD estimates based on the  $\text{O}_2$  difference criterion to be robust and more appropriate particularly for deep convection regions.

### 2.3. Wind Data

[5] The SeaWinds scatterometer on the QuikSCAT satellite was launched in 1999 and delivered wind speed data at global coverage. The highest spatial resolution is 25 km gridded onto a geographical grid of about  $0.25^\circ \times 0.25^\circ$ . In this study, we utilize QuikSCAT wind speed level 3 data (Available at [http://podaac.jpl.nasa.gov/DATA\\_PRODUCT/OVW/index.html](http://podaac.jpl.nasa.gov/DATA_PRODUCT/OVW/index.html)) in our study region from September 2003

to August 2006. The level 3 files contain only the latest measurement for each day with a location accuracy of 10 km (relative). Several studies [e.g., Boutin *et al.*, 2009] demonstrated the good quality of the QuikSCAT wind data ( $\text{RMS} \sim 1 \text{ m s}^{-1}$ ). These wind data were matched with float profiles using the average position between each pair of surfacings. To include information about wind speed variance we also used the 8 neighboring points around this location. The variance of wind speed can have a significant influence on the gas transfer velocity calculated from a nonlinear relationship between gas transfer and wind speed. Long-term winds were obtained by averaging linearly over the 9 grid points at each mean float position as well as over the respective 7 day interval ( $\overline{u_{10}}$ ). In the further analysis dependencies of the gas transfer velocity to the 2nd, 3rd and 4th power of wind speed were calculated. In these, the respective long-term (LT) and short-term (ST) wind speed averages (for 9 pixels  $\times$  7 days) were calculated as follows:

$$u_{10,\text{LT}}^b = (\overline{u_{10}})^b \quad (1)$$

$$u_{10,\text{ST}}^b = \sqrt[b]{\sum \left(\frac{u^b}{n}\right)}, \quad (2)$$

where  $b$  is 2 for the quadratic dependence, 3 for the cubic dependence or 4 for the quartic dependence and  $n$  is the number of observations.

### 2.4. Calibration of Oxygen Data

[6] The raw oxygen data from the optodes were corrected for pressure and salinity using the floats pressure and salinity readings (Aanderaa Manual [Tengberg *et al.*, 2006]) employing the 3.2% per 1000 dbar pressure correction of Uchida *et al.* [2008]. As shown by several other authors [e.g., Körtzinger *et al.*, 2005; Uchida *et al.*, 2008] the factory calibration of the oxygen optodes is generally inadequate. For postcalibration the float oxygen data were compared to oxygen concentrations measured on discrete samples by Winkler titration (accuracy  $< 1.0 \mu\text{mol L}^{-1}$ ). The float and Winkler reference data points were matched in depth space. For float 4900611 the first profile was compared with 7 Winkler samples from R/V Charles Darwin cruise 162 taken 7 days before and in a distance of approx. 17 nm. The oxygen concentrations of float 4900611 were corrected with a linear depth-dependent function yielding corrections ranging from  $23.7 \mu\text{mol L}^{-1}$  (shallow) to  $32.5 \mu\text{mol L}^{-1}$  (deep) with a standard deviation of  $\pm 1.8 \mu\text{mol L}^{-1}$  ( $R^2 = 0.76$ ). For float 4900607 the first profile was compared with a Winkler-calibrated CTD oxygen profile taken 8 days before and in a distance of approx. 20 nm during R/V Meteor cruise 59/3. Float 4900607 was corrected in the same way, i.e., with a linear depth-dependent function yielding corrections ranging from  $11.3 \mu\text{mol L}^{-1}$  to  $21.2 \mu\text{mol L}^{-1}$  with a standard deviation of  $\pm 1.5 \mu\text{mol L}^{-1}$  ( $R^2 = 0.72$ ). Nevertheless, the oxygen optode sensor is long-term stable as shown by Körtzinger *et al.* [2005] and Tengberg *et al.* [2006]. The observed depth dependence of the initial residuals points at the 3.2% depth correction being too low to fully account for the pressure effect on the oxygen measurement. Matching floats and reference data points in density space did not significantly improve the results nor the accuracy of the

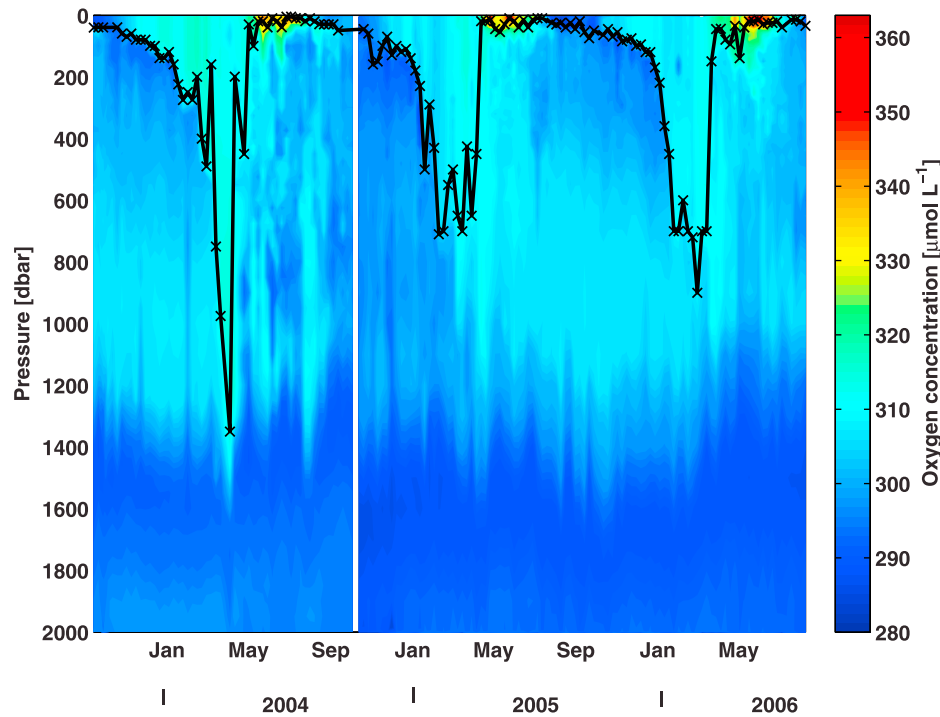


**Figure 2.** Time series of the oxygen concentration of the upper 2000 m in the convection region of the central Labrador Sea (Figure 1). Also shown is the mixed layer depth (black crosses) estimated from the float oxygen profiles using an oxygen criterion of  $\Delta O_2 = 5 \mu\text{mol L}^{-1}$ . The white line indicates the separation between the earlier deployed float 4900607 and the later deployed float 4900611.

correction. Due to the high small-scale variability, oxygen data shallower than 100 dbar were not included in the correction. The remaining residuals between calibrated oxygen float data and the reference data were normally distributed with depth.

## 2.5. Estimation of Gas Transfer Velocity

[7] To estimate the air-sea gas transfer velocity we assumed that the change in the mixed layer oxygen inventory between two consecutive oxygen profiles is primarily driven by air-sea exchange with advection playing only a minor role. During the spring bloom period the mixed layer shoals, promoting phytoplankton growth and oxygen production, resulting in increasing surface oxygen concentrations. During this time of the year the above assumption is clearly violated and the period of the spring bloom was therefore excluded from the further analysis. More precisely, this refers to the period of increasing oxygen concentrations typically found between March and June (21% of all data points were excluded on the basis of this assumption). Gas transfer velocities estimated as described in detail below were also disregarded when the sign of the air-sea  $O_2$  disequilibrium and sign of the change of the oxygen inventory were not the same, e.g., combination of supersaturated surface waters and increase of mixed layer  $O_2$  inventory. These are generally indicative for situations where advective signals dominate (21% of data points excluded). Finally, we also ignored those transfer velocities where the air-sea oxygen disequilibrium, i.e., the thermodynamic driving force of the net gas flux, was  $<1 \mu\text{mol L}^{-1}$  (2% of data points excluded).

[8] The flux of  $O_2$ ,  $F_{O_2}$ , across the air-sea interface can be determined from the bulk equation:

$$F_{O_2} = k_{O_2} \cdot \Delta[O_2], \quad (3)$$

with

$$\Delta[O_2] = [O_2^{sat}] - [O_2^{sea}], \quad (4)$$

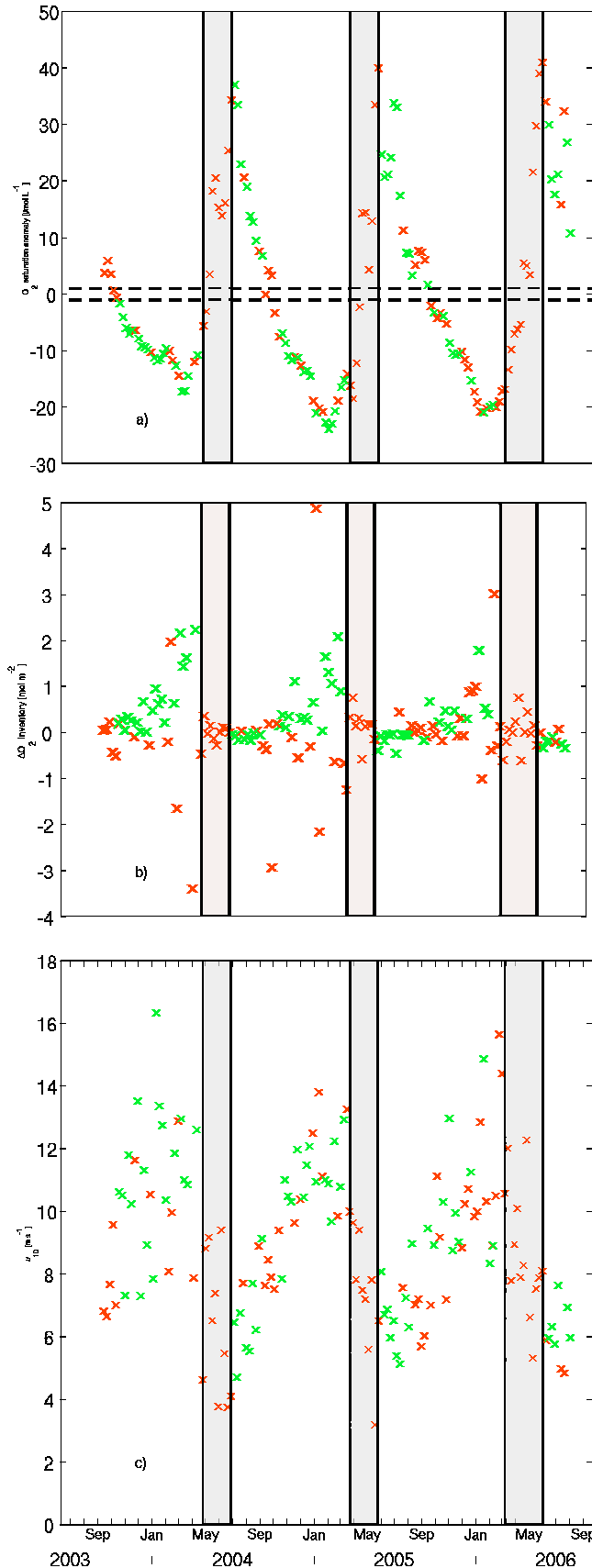
where  $k_{O_2}$  is the transfer velocity for oxygen,  $[O_2^{sea}]$  [Gordon and Garcia, 1992] and  $[O_2^{sat}]$  are the measured and the equilibrium oxygen concentrations of surface seawater. In fact, we used  $\overline{\Delta[O_2]}$ , the mean oxygen disequilibrium between two float profiles ( $n =$  consecutive number of profiles):

$$\overline{\Delta[O_2]} = \frac{(\Delta[O_2]_n + \Delta[O_2]_{n+1})}{2}. \quad (5)$$

[9] If we assume that the  $O_2$  column inventory change in the mixed layer between two consecutive profiles,  $\Delta O_2^{inv}$ , represents the net air-sea oxygen flux  $F_{O_2}$  into or out of the water column, the transfer velocity  $k_{O_2}$  can be calculated using the mean measured air-sea disequilibrium  $\overline{\Delta[O_2]}$ . For this, equation (3) is rearranged and  $\Delta O_2^{inv}$  substituted for  $F_{O_2}$ :

$$k_{O_2} = \frac{F_{O_2}}{\overline{\Delta[O_2]}} = \frac{\Delta O_2^{inv}}{\overline{\Delta[O_2]}}. \quad (6)$$

[10] For the calculation of  $\Delta O_2^{inv}$  we always use the deeper MLD of every pair of  $O_2$  profiles as lower bound of



integration. This makes sure that entrainment fluxes of  $O_2$  during phases of ML deepening as well as a detrainment fluxes of  $O_2$  during phases of ML shoaling are included.

[11] The  $k_{O_2}$  obtained this way (equation (6)) is valid only for the Schmidt number ( $Sc$ ) of oxygen at in situ  $T$  and  $S$  and needs to be scaled to  $k_{660}$ , i.e., the Schmidt number for  $CO_2$  at  $20^\circ C$  in seawater, using equations (7) and (8):

$$k_{660} = k_{O_2} \cdot (Sc/660)^{-1/2} \quad (7)$$

$$Sc = 1953.4 - 128 \cdot T + 3.9918 \cdot T^2 - 0.050091 \cdot T^3. \quad (8)$$

[12] The coefficients in equation (8) are taken from Wanninkhof [1992].

## 2.6. Wind Distribution

[13] For the global wind speed distribution the Rayleigh distribution function is a good approximation. There are, however, regional variances which can influence the relationship between transfer coefficient and long-term wind speed. The use of time-averaged winds leads to an underestimation. The corresponding enhancement factor  $R$ , which expresses the effect of the wind speed distribution on the transfer coefficient in a nonlinear relationship, is given by

$$R = \frac{\sum u^b}{n} / \left( \frac{\sum u}{n} \right)^b, \quad (9)$$

where  $n$  is the number of observations and the exponent  $b$  is 2 for quadratic dependence, 3 for cubic dependence or 4 for quartic dependence. The enhancement factor accounts for the underestimation by a linearly averaged long-term wind in a quadratic, cubic or quartic wind speed dependence of the transfer coefficient.

## 3. Results and Discussion

[14] After correction to within  $1.8 \mu mol L^{-1}$  and  $1.5 \mu mol L^{-1}$  resp. of the Winkler-based oxygen reference we obtained a high-quality oxygen time series of the upper 2000 m in the central Labrador Sea (Figure 2) which shows pronounced seasonality [see also Körtzinger *et al.*, 2008]. The most striking feature is deep convection during wintertime which extends down to depths that vary between 1350 m in winter 2003/2004 and 700–900 m in the two following winters. During these convection periods strong uptake of oxygen from the atmosphere occurs which leads to a rapid buildup of the oxygen inventory down to the maximum convection depth [see also Körtzinger *et al.*, 2004]. It is of interest to note, however, that due to the short time scale of the rapidly deepening convection the mixed layer never reaches equilibrium with the atmosphere but typically stays at  $17\text{--}24 \mu mol L^{-1}$  ( $\sim 5\text{--}7\%$ ) undersaturation (Figure 3a). After

**Figure 3.** (a) Time series of  $O_2$  saturation anomaly, (b)  $O_2$  inventory change between two consecutive profiles ( $\Delta O_2^{inv}$ ), and (c)  $u_{10}$  wind speed. Shown is the complete data set whereas used data are marked in green (see Table 1) and excluded data are marked in red. The gray boxes denote the excluded spring bloom period. Dashed lines represent the  $\pm 1 \mu mol L^{-1}$  envelope. For full description of all criteria used for data selection see section 2.5.

**Table 1.** Final Data Used in This Study to Determine the Air-Sea Gas Transfer Velocity of O<sub>2</sub>

Mixed Layer Depth (m)	$\overline{\Delta[\text{O}_2]}$ ( $\mu\text{mol L}^{-1}$ )	$\Delta\text{O}_2^{mv}$ ( $\text{mmol m}^{-2}$ )	$k_{660}$ ( $\text{cm h}^{-1}$ )
39	1.6	201.4	139.8
60	4.1	287.4	82.2
70	6	54.1	11
60	7	344.4	61.5
79	6.4	270.6	53.7
79	7.8	225	37.3
99	9.2	33.8	4.9
99	9.4	676.9	96.5
139	9.8	11.6	1.6
119	11.2	480.6	58.3
159	11.8	963.7	110.8
224	11.5	621.3	73.5
275	10.5	731.5	95.5
249	9.6	221.9	31.9
400	12.6	640.1	71.7
159	17.3	2165.6	178.6
750	17.1	1442.4	120.2
975	14.4	1632.5	78.7
199	10.7	2242.9	141.9
5	-37.1	-39.2	1.1
9	-33.5	-66.5	2
10	-23	-161.8	7.1
10	-19	-143.4	7.5
20	-13.8	-38	2.7
29	-12.8	-166.7	12.8
30	-9.5	-6.2	0.6
29	-6.8	-49.6	7.4
45	7	146.1	23.6
60	8.7	384.9	51.5
159	10.9	110	12.1
150	11.7	357.1	37.8
69	11.2	1121.5	129.1
100	13.7	304.3	29.3
119	13.5	336.4	33.6
109	14.5	278.4	26.3
179	21	661.7	44.1
289	22.7	39.9	2.5
430	23.9	1655.1	98
710	22.9	1318.4	81.5
700	20.7	1069.8	73.1
500	16.5	2092.7	180
650	15.2	899.1	83.5
19	-24.7	-390.3	19.3
40	-20.7	-72.7	4.2
15	-21.2	-176.6	9.5
40	-24.2	-43	2
15	-33.8	-48	1.5
10	-33.1	-25.1	0.8
10	-17.4	-452.8	12.7
24	-7.3	-46.8	5.8
30	-7.2	-51.6	6.5
25	-3.3	-53.6	15.1
55	-1.6	-167.7	104.1
50	3.3	675.8	112.8
45	3.9	225.2	69.4
55	8.6	482.9	70
84	10.4	143.1	17.8
79	10.8	61.8	7.5
75	10.5	477.8	60.4
119	15.3	302.9	27.2
450	20.9	1790.6	120.8
700	19.9	537.3	37.6
600	19.6	399.6	28.7
24	-30	-335.3	13.1
25	-20.3	-186.9	10.2
20	-17.6	-184.4	11.1
40	-21.2	-96	2.3
15	-26.8	-243.7	8.9
20	-10.8	-332.5	29.5

cessation of the convection activity the convectively mixed volume is almost instantly sealed from atmospheric contact by a rapidly forming warm and fresh (sea ice meltwater) surface layer (data not shown). In this layer the spring bloom soon forms which causes production of oxygen and depletion of winter time nutrient concentrations. As a consequence the mixed layer changes from undersaturated to strongly supersaturated by up to 37–41  $\mu\text{mol L}^{-1}$  (~15%) for oxygen. This period of strong in situ oxygen formation was entirely excluded from our analysis as air-sea exchange is not the dominant effect anymore for changes in the mixed layer oxygen inventory (Figure 3b). After depletion of surface nutrients the spring bloom decays and the oxygen supersaturation is gradually reduced by air-sea exchange and the effect of surface cooling. The mixed layer again turns back to undersaturated when it starts deepening toward the end of the year (Figure 3). The subsurface waters underneath the shallow summer mixed layer show clear sign of a strong respiration signal which mirrors the remineralization of a major fraction of the summer export production in the overlying waters (Figure 2). This evolving seasonal subsurface oxygen deficit is a major driver for the strong oxygen fluxes into the ocean in the following deep convection period. Following the approach and selection criteria outlined in section 2 we yielded a total of 69 estimates of the oxygen flux for 7 day periods bracketed by two consecutive oxygen profiles (see Table 1). By calculating the average air-sea oxygen disequilibrium of these pairs of profiles we were able to calculate the apparent transfer velocities for oxygen. Using the temperature-dependent Schmidt number for oxygen and a square root Schmidt number dependence of  $k$ , these transfer velocities were scaled to the transfer velocity of CO<sub>2</sub> in seawater at 20°C and a salinity of 35 ( $k_{660}$ ). These estimates of the transfer velocity were then matched with the QuickSCAT wind speed data for the respective locations and time periods to investigate their wind speed dependence. This dependence was explored in two different ways representing different types of wind speed data. For long-term winds, i.e., wind speed averaged linearly over periods of weeks to months, all wind speed data points (9 pixels  $\times$  7 days = 63 data points) were averaged into a single arithmetic mean wind speed. However, as shown in Figure 4, the daily wind speed was highly variable and varied between 0.24 and 28.6  $\text{m s}^{-1}$  with an average wind speed of  $9.0 \pm 4.6 \text{ m s}^{-1}$ . For short-term winds, the full wind speed distribution of the respective period was retained by calculating the average wind speed using a quadratic, cubic or quartic dependence (equation (2)). The estimated air-sea gas transfer velocity  $k_{660}$ , separated into four seasons, and the quadratic, cubic and quartic relationships for long-term winds are shown in Figure 5. At the end of spring and in early summer the central Labrador Sea is characterized by comparatively low wind speed, shallow mixed layers, supersaturation of oxygen and small changes in mixed layer oxygen inventory resulting in low gas transfer velocities and evasion. In contrast, the later winter situation is characterized by strong winds, deep mixed layers, general undersaturation of oxygen and high O<sub>2</sub> inventory changes resulting in high transfer velocities and high O<sub>2</sub> invasion. To these data quadratic, cubic and quartic fit functions (forced through origin) were calculated (Table 2). For clarity all results were binned into 1  $\text{m s}^{-1}$  intervals (Figure 6). It becomes apparent that the quadratic fit functions significantly

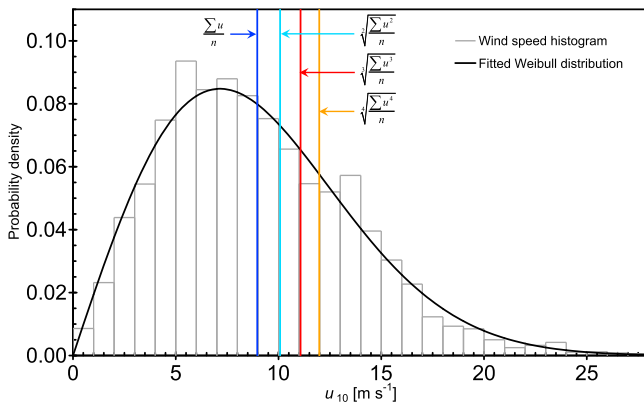


**Figure 4.** Distribution of QuickSCAT winds over the central Labrador Sea during the period September 2003 to August 2006 as well as the probability density according to a Weibull function with shape parameter  $k = 2$  (Rayleigh function). Also shown are wind averages for a linear, quadratic, cubic, and quartic dependence.

overestimates  $k_{660}$  at  $u_{10} < 9 \text{ m s}^{-1}$  while it performs reasonably well at  $u_{10} > 9 \text{ m s}^{-1}$ . The stronger curvature of the cubic dependence clearly fits the lower wind speed range better. There is some indication, however, that at very high wind speed the cubic fit yields for high  $k$  values. It needs to be pointed out, however, that for the two highest wind speed only single data points are available which makes their statistic weight rather small compared to averages provided elsewhere. Using a quartic fit does not improve the overall fit but in fact makes it weaker. The quadratic, cubic and quartic parameterizations of  $k_{660}$  are compared with the prominent of *Liss and Merlivat* [1986], *Wanninkhof* [1992], *Wanninkhof and McGillis* [1999], *Nightingale et al.* [2000], and *Sweeney et al.* [2007] (hereafter referred to as LM86, W92, WM99, N00, and S07). For short-term winds, the quadratic

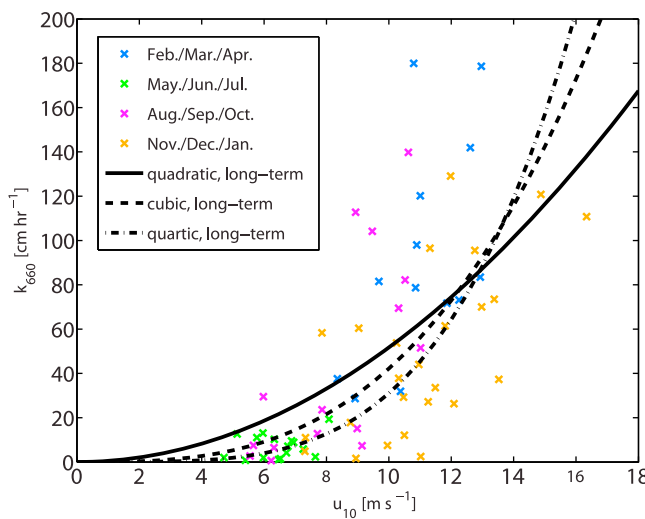


**Figure 5.** Estimated gas transfer velocity  $k_{660}$  versus long-term wind speed separated into four seasons: FMA, MJJ, ASO, and NDJ. The lines represent the quadratic (solid), cubic (dashed), or quartic (dash-dotted) functions fitted to the data.

**Table 2.** Compilation of the Coefficient  $a$  in  $k = a u_{10}^b$  as Estimated in This Study<sup>a</sup>

Parameter	Quadratic Approximation	Cubic Approximation	Quartic Approximation
Long-term wind	0.52 ( $\pm 0.04$ )	0.042 ( $\pm 0.003$ )	0.0031 ( $\pm 0.0003$ )
Short-term wind	0.44 ( $\pm 0.03$ )	0.029 ( $\pm 0.002$ )	0.0016 ( $\pm 0.0001$ )
Enhancement factor R	1.16	1.48	1.94

<sup>a</sup>Standard errors in parentheses. Also given is the enhancement factor R.

function shows much stronger wind speed dependence than W92, N00, and S07 which is partly an effect of the overestimation at low/intermediate wind speed. The cubic function falls almost exactly on top of the WM99 parameterization (Figure 7a). The quartic function yields the lowest  $k_{660}$  values of all parameterizations at  $u_{10} < 10 \text{ m s}^{-1}$ . For long-term winds, the quadratic fit also shows stronger wind speed dependence of  $k_{660}$  than W92 whereas the cubic fit yields  $k_{660}$  values that fall below WM99. Again the quartic function yields the lowest of all  $k_{660}$  values at  $u_{10} < 11 \text{ m s}^{-1}$  (Figure 7b). The period of low wind speed ( $< 9 \text{ m s}^{-1}$ ) is generally characterized by supersaturated surface water and low gas transfer velocities, whereas undersaturated surface water with high gas transfer velocities are accompanied by high wind speeds ( $> 9 \text{ m s}^{-1}$  up to  $16 \text{ m s}^{-1}$ , Figure 8). Both theoretical and experimental studies suggest that at high wind speed there is an enhancement in gas transfer velocities in the upper ocean by bubble injection through breaking waves. Uncertainties still exist as to by which mechanism breaking waves enhance air-sea gas exchange [*Woolf*, 2005]. It is generally known that significant supersaturation of gases is found at higher wind speeds. For oxygen the supersaturation mediated by bubble entrainment exceeded 1% at wind speeds of  $> 9 \text{ m s}^{-1}$ . For  $\text{CO}_2$  the 1% supersaturation occurs only at much higher wind speed of  $> 49 \text{ m s}^{-1}$  [*Woolf and Thorpe*, 1991]. Therefore oxygen will be affected toward higher wind speed in our data set such that the estimated

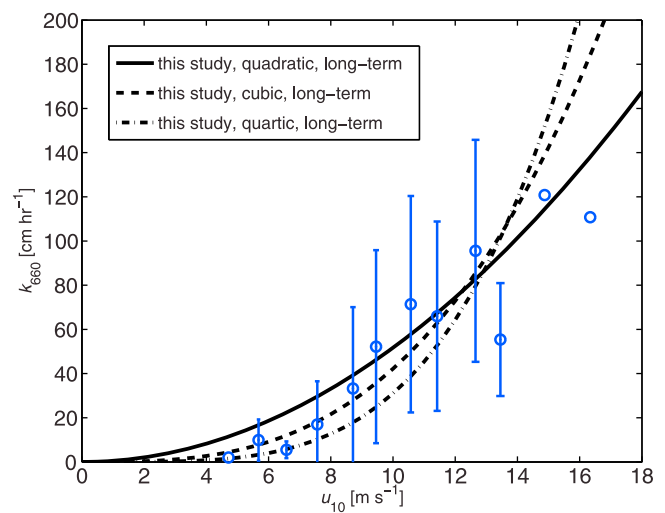


**Figure 6.** Estimated gas transfer velocities, bin averaged in  $1 \text{ m s}^{-1}$  intervals, (blue circles) with standard deviation (circles with standard deviation are single values). The lines represent the quadratic (solid), cubic (dashed) or quartic (dash-dotted) fits.

transfer velocities in this range will be slightly biased high. This causes an artifact when converted to  $k_{660}$  for  $O_2$  since this gas is essentially unaffected by bubble entrainment. Bubble entrainment correction after *Woolf and Thorpe* [1991] reduce the coefficient  $a$  for the quadratic dependence (see Table 2) by 29.4%. The enhancement factors obtained here for quadratic,

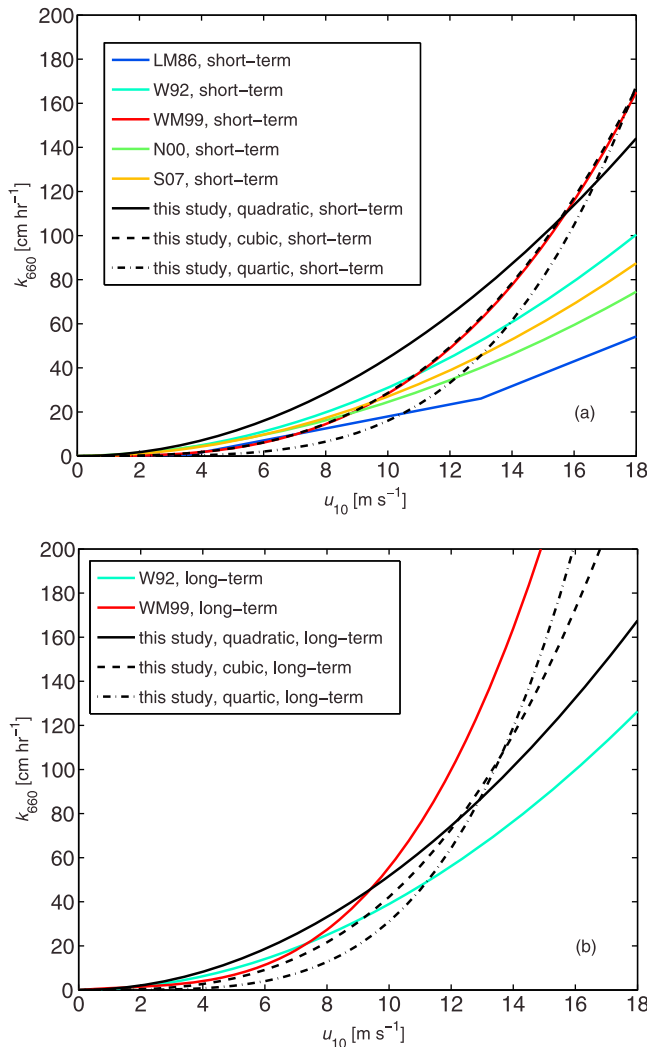


**Figure 7.** Comparison of fits for (a) short-term winds and (b) long-term winds with prominent parameterizations from the literature. The latter include the relationships of *Liss and Merlivat* [1986], *Wanninkhof* [1992], *Wanninkhof and McGillis* [1999], *Nightingale et al.* [2000], and *Sweeney et al.* [2007] (hereafter referred to as LM86, W92, WM99, N00, and S07) for Figure 7a and *Wanninkhof* [1992] and *Wanninkhof and McGillis* [1999] for Figure 7b. Shown in Figure 7a are the short-term relationships obtained in this study, where the solid black line ( $k = 0.44 u_{10}^2$ ) is the quadratic relationship, the dashed black line ( $k = 0.029 u_{10}^3$ ) is the cubic relationship, and the dash-dotted black line ( $k = 0.0016 u_{10}^4$ ) is the quartic relationship. In Figure 7b, the solid black line ( $k = 0.52 u_{10}^2$ ) is the quadratic relationship, the dashed black line ( $k = 0.042 u_{10}^3$ ) is the cubic relationship, and the dash-dotted line ( $k = 0.0031 u_{10}^4$ ) is the quartic relationship obtained for long-term winds in this study. All data were normalized to  $Sc = 660$ .

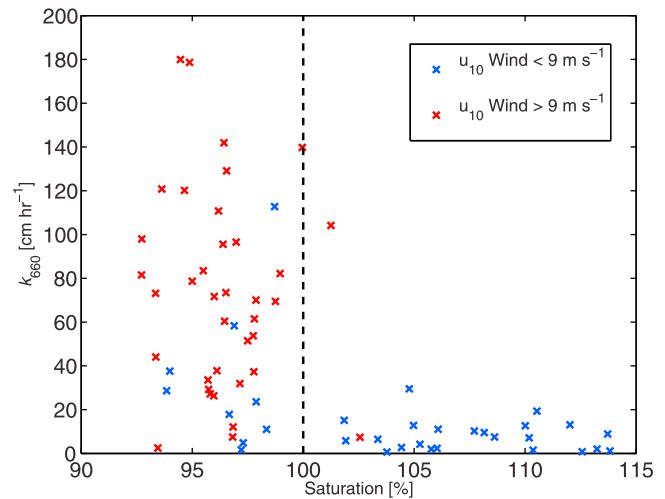


**Figure 8.** Distribution of air-sea gas transfer velocities  $k_{660}$  versus oxygen saturation. High gas transfer velocities are associated with undersaturated surface water and high wind speed ( $>9 \text{ m s}^{-1}$  up to  $16 \text{ m s}^{-1}$ ), while supersaturated surface water and low wind speed ( $<9 \text{ m s}^{-1}$ ) are associated with low gas transfer velocities.

cubic and quartic wind speed dependencies (Table 2) are very similar to the ones calculated by *Wanninkhof et al.* [2002] using a Rayleigh wind speed distribution and 6 h wind speed data. Our wind speed data (Figure 4) can indeed be approximated well by a Rayleigh function, i.e., a special form of the Weibull function where the shape parameter  $k = 2$ .

[15] In summary, we were able to constrain the wind speed dependence of the transfer velocity for air-sea gas exchange of  $O_2$  by oxygen time series measured from profiling floats in the Labrador Sea. In general, our results show wind speed dependencies that lie in the upper band of prominent parameterizations. Also, the stronger curvature of cubic dependencies fits the observations better than quadratic ones pointing at the importance of high wind speed for air-sea gas exchange.

[16] **Acknowledgments.** This study was supported by the Deutsche Forschungsgemeinschaft (DFG) through SFB 460. It was also funded through the integrated project CarboOcean under the 6th framework programme of the European Commission.

## References

- Boutin, J., Y. Quilfen, L. Merlivat, and J. F. Piolle (2009), Global average of air-sea  $CO_2$  transfer velocity from QuickSCAT scatterometer wind speeds, *J. Geophys. Res.*, *114*, C04007, doi:10.1029/2007JC004168.
- Gordon, H. E., and L. I. Garcia (1992), Oxygen solubility in seawater: Better fitting equations, *Limnol. Oceanogr.*, *37*(6), 1307–1312.
- Körtzinger, A., J. Schimanski, U. Send, and D. W. R. Wallace (2004), The ocean takes a deep breath, *Science*, *306*(5700), 1337.
- Körtzinger, A., J. Schimanski, and U. Send (2005), High-quality oxygen measurements from profiling floats: A promising new technique, *J. Atmos. Oceanic Technol.*, *22*, 302–308.
- Körtzinger, A., U. Send, D. W. R. Wallace, J. Karstensen, and M. DeGrandpre (2008), Seasonal cycle of  $O_2$  and  $pCO_2$  in the central Labrador Sea: Atmospheric, biological, and physical implications, *Global Biogeochem. Cycles*, *22*, GB1014, doi:10.1029/2007GB003029.
- Liss, P. S., and L. Merlivat (1986), Air-sea gas exchange rates: Introduction and synthesis, in *The Role of Air-Sea Exchange in Geochemical Cycling*, edited by P. Buat-Ménard, pp. 113–127, D. Reidel, Dordrecht, Neth.

- Monterey, G., and S. Levitus (1997), Seasonal variability of mixed layer depth for the World Ocean, *NOAA Atlas NESDIS 14*, 96 pp., NOAA, Washington, D. C.
- Nightingale, P. D., G. Malin, C. S. Law, A. J. Watson, P. S. Liss, M. I. Liddicoat, J. Boutin, and R. C. Upstill-Goddard (2000), In situ evaluation of air-sea gas exchange parameterizations using novel conservative and volatile tracers, *Global Biogeochem. Cycles*, *14*(1), 373–387, doi:10.1029/1999GB900091.
- Sweeney, C., E. Gloor, A. R. Jacobson, R. M. Key, G. McKinley, J. L. Sarmiento, and R. Wanninkhof (2007), Constraining global air-sea exchange for CO<sub>2</sub> with recent bomb <sup>14</sup>C measurements, *Global Biogeochem. Cycles*, *21*, GB2015, doi:10.1029/2006GB002784.
- Tengberg, A., et al. (2006), Evaluation of a life time based optode to measure oxygen in aquatic systems, *Limnol. Oceanogr. Methods*, *4*, 7–17.
- Uchida, H., T. Kawano, I. Kaneko, and M. Fukasawa (2008), In situ calibration of optode-based oxygen sensors, *J. Atmos. Oceanic Technol.*, *25*, 2271–2281.
- Wanninkhof, R. (1992), Relationship between wind-speed and gas exchange over the ocean, *J. Geophys. Res.*, *97*, 7373–7382, doi:10.1029/92JC00188.
- Wanninkhof, R., and W. R. McGillis (1999), A cubic relationship between air-sea CO<sub>2</sub> exchange and wind speed, *Geophys. Res. Lett.*, *26*, 1889–1892.
- Wanninkhof, R., S. C. Doney, T. Takahashi, and W. R. McGillis (2002), The effect of using time-averaged winds on regional air-sea CO<sub>2</sub> fluxes, in *Gas Transfer at Water Surfaces*, *Geophys. Monogr. Ser.*, vol. 127, edited by M. A. Donelan et al., pp. 351–356, AGU, Washington, D. C.
- Woolf, D. K. (2005), Parametrization of gas transfer velocities and sea-state dependent wave breaking, *Tellus Ser. B*, *57*, 87–94.
- Woolf, D. K., and S. A. Thorpe (1991), Bubbles and the air-sea exchange of gases in near-saturation conditions, *J. Mar. Res.*, *49*, 435–466.

---

C. Kihm and A. Körtzinger, Leibniz-Institut für Meereswissenschaften an der Universität Kiel, Düsternbrooker Weg 20, D-24105 Kiel, Germany. (ckihm@ifm-geomar.de; akoertzinger@ifm-geomar.de)